Limits of oxygen isotope palaeoaltimetry in Tibet

Earth and Planetary Science Letters 606 (2023) 118040

Contents lists available at ScienceDirect

Earth and Planetary Science Letters

journal homepage: www.elsevier.com/locate/epsl

Limits of oxygen isotope palaeoaltimetry in Tibet

Alex Farnsworth [a,b,*], Paul J. Valdes [b], Lin Ding [a,f], Robert A. Spicer [a,c,d], Shi-Hu Li [e,f], Tao Su [c,g], Shufeng Li [c,g], Caitlyn R. Witkowski [h], Zhongyu Xiong [a]

[a] State Key Laboratory of Tibetan Plateau Earth System, Resources and Environment (TPESRE), Institute of Tibetan Plateau, Chinese Academy of Sciences, Beijing, China
[b] School of Geographical Sciences and Cabot Institute, University of Bristol, Bristol, BS8 1SS, UK
[c] CAS Key Laboratory of Tropical Forest Ecology, Xishuangbanna Tropical Botanical Garden, Chinese Academy of Sciences, Mengla 666303, China
[d] School of Environment, Earth and Ecosystem Sciences, The Open University, Walton Hall, Milton Keynes, MK7 6AA, UK
[e] State Key Laboratory of Lithospheric Evolution, Institute of Geology and Geophysics, Chinese Academy of Sciences, Beijing, 100029, China
[f] Lancaster Environment Centre, University of Lancaster, LA1 4YQ, UK
[g] University of Chinese Academy of Sciences, Beijing 100049, China
[h] School of Earth Sciences and Cabot Institute, University of Bristol, Bristol, BS8 1SS, UK

ARTICLE INFO

Article history:
Received 28 April 2022
Received in revised form 30 January 2023
Accepted 2 February 2023
Available online 24 February 2023
Editor: Y. Asmerom

Keywords:
palaeoclimate
palaeoaltimetry
Tibet
isotope
modelling
Eocene

ABSTRACT

Measurements of stable water isotopes (oxygen and hydrogen) are commonly used to estimate palaeoelevation and quantify past changes in surface height across Tibet. Isotope palaeoaltimetry is often based on simple Rayleigh fractionation of a "parcel of air", but must make a considerable number of approximations and assumptions. In this paper, we elaborate on the practicability of oxygen water isotopes in palaeoaltimetry, and evaluate a recent challenge to the palaeoaltimetry community. First, we examine the isotopic composition of oxygen ($\delta^{18}O$) versus altitude relationship in a set of five topographic realisations of Tibet using an isotope-enabled palaeoclimate model for the mid-Eocene, a period where a variety of topographic 'uplift' models have been proposed, and compare it to modern relationships. Second, we investigate whether isotopic composition is a good predictor of more modest changes in topography, such as the introduction of a valley system or uplift of only part of the Tibetan region. The aim of the paper is not to perform a direct comparison to data, but to use the model to further refine knowledge of the strengths and limitations of using oxygen isotopes in palaeoaltimetry. We find that oxygen isotope palaeoaltimetry works surprisingly well, with the exception that it could not identify low elevation valley systems bounded by high elevations because the isotopic composition of the water in the air becomes depleted at the first high elevation that an air parcel passes over and does not recover when it descends into the valley. Hence, isotope-based elevations are biased towards mountain range peaks. Overall, the application of oxygen isotope palaeoaltimetry does have value, but would be further strengthened when employed together with isotope-enabled models. In conjunction with other techniques such as terrestrial thermal lapse rates and energy conservation approaches, over a wide spatial region, a more accurate and fully three-dimension view of complex palaeo-topography is increasingly possible, which will in turn improve the precision of these palaeoaltimeters.

1. Introduction

Knowing accurately the elevation history of Tibet (and other uplands) has the potential to improve our understanding of plate dynamics (Brenner et al., 2020; Lippert et al., 2011), core-mantle interactions (Li and Song, 2018; Xiong et al., 2022), the geophysical structure of Earth (Jellinek et al., 2020) and climate dynamics (Farnsworth et al., 2019). Surface height has, for a considerable time, been identified as an important boundary condition for climate models in that it has a major impact on atmospheric and ocean circulation patterns, both locally, regionally (e.g. Ehlers and Poulsen, 2009; Farnsworth et al., 2019; Gregory-Wodzicki et al., 1998; Huber and Goldner, 2012; Li et al., 2021; Molnar et al., 2010; Walsh, 1994) as well as globally (Yang et al., 2020). Furthermore, how these processes interact to shape the landscape is important to understand due to their wider impact on biodiversity patterns through time (Li et al., 2021; Saupe et al., 2019).

Estimating palaeoelevation with any accuracy and precision is difficult (Farnsworth et al., 2021; Meyer, 2007; Spicer et al., 2021a).

* Corresponding author.
E-mail address: alex.farnsworth@bristol.ac.uk (A. Farnsworth).

https://doi.org/10.1016/j.epsl.2023.118040

Simple understanding of plate tectonics can help strengthen our qualitative knowledge of uplift history by allowing us to estimate the location (e.g. Markwick and Valdes, 2004) major mountain ranges, erosion, sediment mobilization and accumulation (e.g. Zhang et al., 2019). However, what is really required is a way of measuring directly the elevation of Earth's surface, but reliable quantification of palaeoelevation is problematic and has to be done via a range of proxies.

Such proxies are typically in the form of either fossils or isotopic composition. To convert temperature-based estimates derived from fossils, often but not exclusively plants, through morphological leaf trait analysis (e.g. Spicer et al., 2021c) or taxonomic affiliation, (e.g. Deng and Ding, 2015; Utescher et al., 2014) requires knowledge of thermal lapse rates that show large variation range and cannot be constrained from proxy observations, but may be derived from climate models (e.g. Farnsworth et al., 2019; Su et al., 2019). Leaf-trait analysis methods can also be used to estimate moist enthalpy from which elevation can be estimated through conservation of energy principles (Forest et al., 1995), but this requires an estimate of moist enthalpy at mean sea level at the same geological time, and similar latitude. When proximal co-eval sea level fossil assemblages are not available, models can also be used to estimate such values (Khan et al., 2014; Su et al., 2020).

Palaeoelevation estimates can also be derived using stable water (oxygen and hydrogen) isotope signatures preserved in proxies (e.g. as carbonates in palaeosols, hydrothermally altered minerals, metamorphic micas, clay minerals, fossil teeth, chert, hydrated volcanic glasses) (e.g. Garzione et al., 2000; Polissar et al., 2009; Rowley and Currie, 2006) by exploiting isotope fractionation that takes place through atmospheric processes. This approach has been extensively used to estimate Tibetan orographic history (see review in: Ding et al., 2017). Stable isotope palaeoaltimetry assumes that stable water isotopes undergo Rayleigh fractionation as moisture is lofted over a mountain. Heavy ^{18}O and D isotopes preferentially rain out first and thus decrease the isotopic composition values (with respect to δ^{18}O and δD) with increasing distance from the original water source. To quantify this isotopic change, the isotopic composition of the original water source is required, i.e., the water at the base of the mountain where the ascent begins. In the geologic record, these stable water isotopes are then archived in a secondary geologic material (e.g., carbonates, organic matter) that is presumed to accurately reflect the isotopic values of precipitation (Rowley, 2007). Assuming that the archive is not altered during diagenesis, the stable water isotope method assumes that there is no significant recycling of moisture along the air parcel trajectory or convergence of other air parcels from geographically remote moisture sources.

These assumptions regarding air parcel physics (e.g., moisture recycling or convergence) can be evaluated using stable water isotope-enabled climate models that incorporate a much more complex and complete representation of fractionation processes as compared to the very simple treatment or even 'educated guesses' (Hoke, 2018) often used in the exclusively proxy-based approach. Many publications have investigated the relationship between stable water isotopes and altitude via isotope-enabled models as applied to S. American and N. American orography (Feng et al., 2013; Poulsen et al., 2010). These papers concluded that many factors influence the δ^{18}O signal in precipitation, including changes in vapour mixing, source regions, moisture recycling, and precipitation type (i.e., convective versus large-scale). The different impacts of convective and large-scale precipitation on the isotopic composition of rainwater were first noted by Dansgaard (1964). Dansgaard observed that higher latitude samples (dominated by large scale precipitation) had a greater correlation between the isotopic content and air temperature compared to the tropics (dominated by convective precipitation) and sub-tropics, which had greater depletion in heavier water isotopes due to higher precipitation rates. The process became known as the "amount effect". Terrestrial sources of fractionation (e.g. different vegetation types can have different transpiration fluxes as a result of different water use efficiency strategies and these can result in different fractionation rates that can impact the oxygen isotope signature (Farquhar et al., 2007)) may also be a factor that is currently not considered in some models. However, it is likely to be of secondary importance as soil evaporation (which includes transpiration in the land surface scheme in HadCM3) only accounts for 10% (Tindall et al., 2009) of total evaporation from the land surface scheme, where fractionation in the soil column is accounted for.

More recently, Botsyun et al. (2016) evaluated δ^{18}O versus altitude relationships for Tibet. They performed a series of simulations with modern day geographic configuration and varied the height and distribution of Tibetan elevation. Using their isotope-enabled climate model they concluded that only about 40% of sampled sites reflected the topographic signal, that humidity-related changes altered the relationship in northern Tibet and precipitation amount effects impacted to the south (Tharammal et al., 2017). Similarly, Shen and Poulsen (2019) showed that the Rayleigh distillation process is only dominant in the monsoonal regions of the Himalaya when the mountains are high. Both studies argue that the stable water isotope altimetry has severe limitations when applied to the Himalayan-Tibetan region.

However, neither of these studies modified their palaeogeography nor considered the past complex topography of Tibet. The simulations were simply sensitivity experiments using modern-day geography. So far, the only isotope-enabled model study of Tibetan δ^{18}O values versus altitude relationships with a palaeo-configuration was by Botsyun et al. (2019). They simulated hypothetical mid-Eocene conditions using variously elevated modern plateau heights and compared the outcomes to observational δ^{18}O data constraints. They concluded that the best match between models and data could only be achieved if Eocene elevations were very low. Their best match was when the entire Tibetan region was less than 1000 m high, which is at odds with proxy-constraints (Ding et al., 2014; Ingalls et al., 2017) and a wealth of geological arguments for the formation of a high Andean-type Gangdese mountain system in the south of the Tibetan region arising from the successive subduction of Neo-Tethys Oceanic crust and indentation of India onto Eurasia (Kapp and DeCelles, 2019). Valdes et al. (2019) have challenged the Botsyun et al. (2019) conclusion, suggesting that their atmosphere-only model could be seriously biasing their results and that the sea-surface temperatures they used were anomalously warm.

In this paper, we will elaborate on the practicability of oxygen water isotope in palaeoaltimetry in two respects. First, we will evaluate the δ^{18}O versus altitude relationship of our mid-Eocene simulation and compare it to modern relationships. Second, we will then investigate whether the isotopic distribution is a good predictor of more modest changes in topography, such as the introduction of a valley system or uplift of only part of the Tibetan region. The aim of the paper is not to perform a direct comparison to observational data because we are not necessarily reproducing realistic past landscapes and until realistic landscapes are included such comparisons would be invalid, but to use the model to further refine the strengths and limitations of stable water isotopes in palaeoaltimetry, in particular the use of oxygen isotopes fractionation. Similarly, the processes that cause the breakdown of a strong elevation – oxygen isotope relationship have been well described in various papers (Deng and Ding, 2015; Hoke, 2018; Jing et al., 2022; Moore et al., 2014; Poage and Chamberlain, 2001; Quade et al., 2011; Shen and Poulsen, 2019; Spicer et al., 2021b; Tharammal et al., 2017; Valdes et al., 2019; Xiong et al., 2022), so we aim to examine the typical uncertainty associated with the technique.

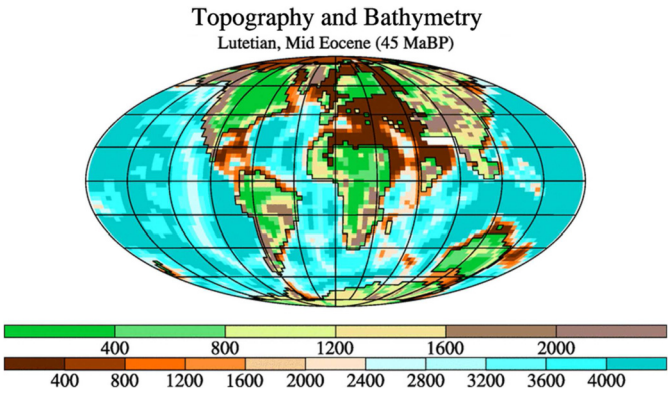

Fig. 1. Model resolution palaeogeographic reconstruction (land-sea mask, land elevation, ocean bathymetry) for the Lutetian (41-48 Ma, average 45 Ma). Contours represent bathymetric depth and topographic height (m).

2. Methods

We use the isotope-enabled version of the HadCM3L climate model (HadCM3BL-M2.1aD, using the nomenclature in Valdes et al., 2017). This model has a horizontal resolution of $3.75^{\circ} \times 2.5^{\circ}$ in longitude/latitude respectively, has 19 levels in the atmosphere, and has 20 levels in the ocean. As such, it uses a lower resolution than that of Botsyun et al. (2019) or Shen and Poulsen (2019). This means that the model cannot represent well the very fine details of topography and would therefore not be as good for modern scenarios. However, details of ancient topography are not defined at high spatial resolution for palaeo reconstructions (and are, after all, what we are trying to determine), so the lower resolution is not a serious limitation. This resolution is sufficient to capture major palaeofeatures such as a wide (∼300 km) Central Tibetan Valley (e.g. Su et al., 2020; Xiong et al., 2022).

The isotope module is identical to that published in Tindall et al. (2010) except for some small changes to the numerical scheme to improve model stability. In addition, we change the ozone scheme in the model. In the original pre-industrial simulation of HadCM3BL, the ozone distribution is prescribed as a latitude-pressure-time distribution. However, experience (Valdes et al., 2021) has shown that for warm climates the tropopause rises and stratospheric ozone penetrates into the troposphere, which is unphysical. We therefore replace the 3-D ozone distribution scheme with a simple dynamic one in which ozone is coupled to the model's tropopause height and use constant values for the troposphere (0.02 ppm), tropopause (0.2 ppm), and stratosphere (5.5 ppm). This change makes a negligible difference to the global mean surface temperature, but does have a small impact on the stratospheric temperature (~ -6 °C in the pre-industrial simulation) and winds (~ -8 m/s for the pre-industrial).

We change the model boundary conditions so they are configured for the mid-Eocene, specifically the Lutetian (41-48 Ma). This consists of reducing the solar constant by 0.4%, increasing the atmospheric CO_2 concentration to 840 ppmv (3x pre-industrial) (Foster et al., 2017), and the baseline palaeogeography to that in Lunt et al. (2016). Fig. 1 shows this palaeogeographic reconstruction. Other radiatively active gases, aerosols, and orbital parameters are unchanged from modern conditions. We refer to this simulation as our "control" mid-Eocene condition. Note that in this palaeogeography there is a shallow (<50 m) ocean between continental India and Eurasia. The width or even existence of such an ocean is a topic of considerable debate, particularly following recent documentation of Eurasian sediments on the Indian plate as early as 61 Ma (An et al., 2021). Until that discovery, the consensus view was that continent-continent collision began at 55±10 Ma (Wang et al., 2014) and so this reconstruction is perhaps less contentious than a full land connection in the Lutetian.

We also perform four sensitivity simulations with much smaller changes to the elevations in Tibet. In the "control" simulation, we change these profiles in the following ways:

- Scenario 1 (the "control"): Gangdese mountains are low (∼2000 m) and the Qiangtang (Tanggula or Central Watershed) range at 4000 m, using unmodified Getech palaeogeography.
- Scenario 2: Gangdese mountains are set at 4500 m high, the Qiangtang range at 4000 m, and a valley between them at 1500 m (e.g. Su et al., 2019).
- Scenario 3: Same as Scenario 2, but the valley is set at 4000 m, using a high 'proto-plateau' configuration (e.g. Rowley and Currie, 2006; Wang et al., 2008).
- Scenario 4: Gangdese mountains are set at 1500 m high, the Qiangtang range at 4500 m, and the region between them at 1500 m (e.g. Molnar, 2005).
- Scenario 5: Gangdese mountains are set at 2000 m high, the Qiangtang range at 2000 m, and the region between them at 2000 m, using a low 'proto-plateau' configuration. (e.g. Botsyun et al., 2019).

The resulting elevation changes and profiles are shown in Fig. 2.

All simulations were initialised from a previous Lutetian simulation, which had been spun-up without isotope tracking enabled for more than 3000 years. All isotope simulations were run for 500 years, with the last 100 years used to form climatological means. This was sufficient for the surface ocean temperature to reach near equilibrium, but the deep ocean temperature is still trending. We therefore concentrate on the surface ocean (and atmosphere) only.

3. Results - pre-industrial model evaluation

Although the pre-industrial isotope-enabled model has been published (Tindall et al., 2009) and generally tested against observations, previous evaluation studies have not focused on the Asian region, and in particular not Tibet. Therefore, in Fig. 3a we show a comparison of the GNIP modern observational data ((Global Network of Isotopes in Precipitation (GNIP), 2019), interpolated onto the same resolution as HadCM3L) with our pre-industrial simulation (Fig. 3b, c). Overall, the Pre-industrial model performs well compared to the GNIP $\delta^{18}O$ observations, capturing the generally heavier $\delta^{18}O$ values to the west and the lighter $\delta^{18}O$ values to the east. The few observational values over Tibet are also captured although those generated by the model are not as low as those observed. This may be due to the coarse resolution of HadCM3L, which does not capture the high elevations of the Himalaya.

Further confirmation of the performance of the pre-industrial HadCM3L simulation is shown in Fig. 4. This shows the seasonal cycle of observations and those seen in the model for New-Delhi and Lhasa. In both cases, the model and data compare reasonably well. For New Delhi, the modelled seasonal cycle is simulating the onset of the Indian monsoon approximately one month earlier than the observations (May as opposed to mid-June). In reality, the onset of the monsoon is highly variable compared to the climatological onset. A similar shift is also seen in precipitation. For Lhasa, the modelled amplitude of the cycle is less marked than in the observations (potentially due to the lower Himalaya as a result of the spatial resolution in the model), but in both cases, the annual means are approximately correct. A further explanation for the less marked modelled amplitude may be the length of the reporting period for the GNIP Lhasa site. In general, the GNIP reporting period(s) are in the order of years, and not decades. This makes these sites more susceptible to interannual variations in weather patterns that can influence the $\delta^{18}O$ and δD. For example,

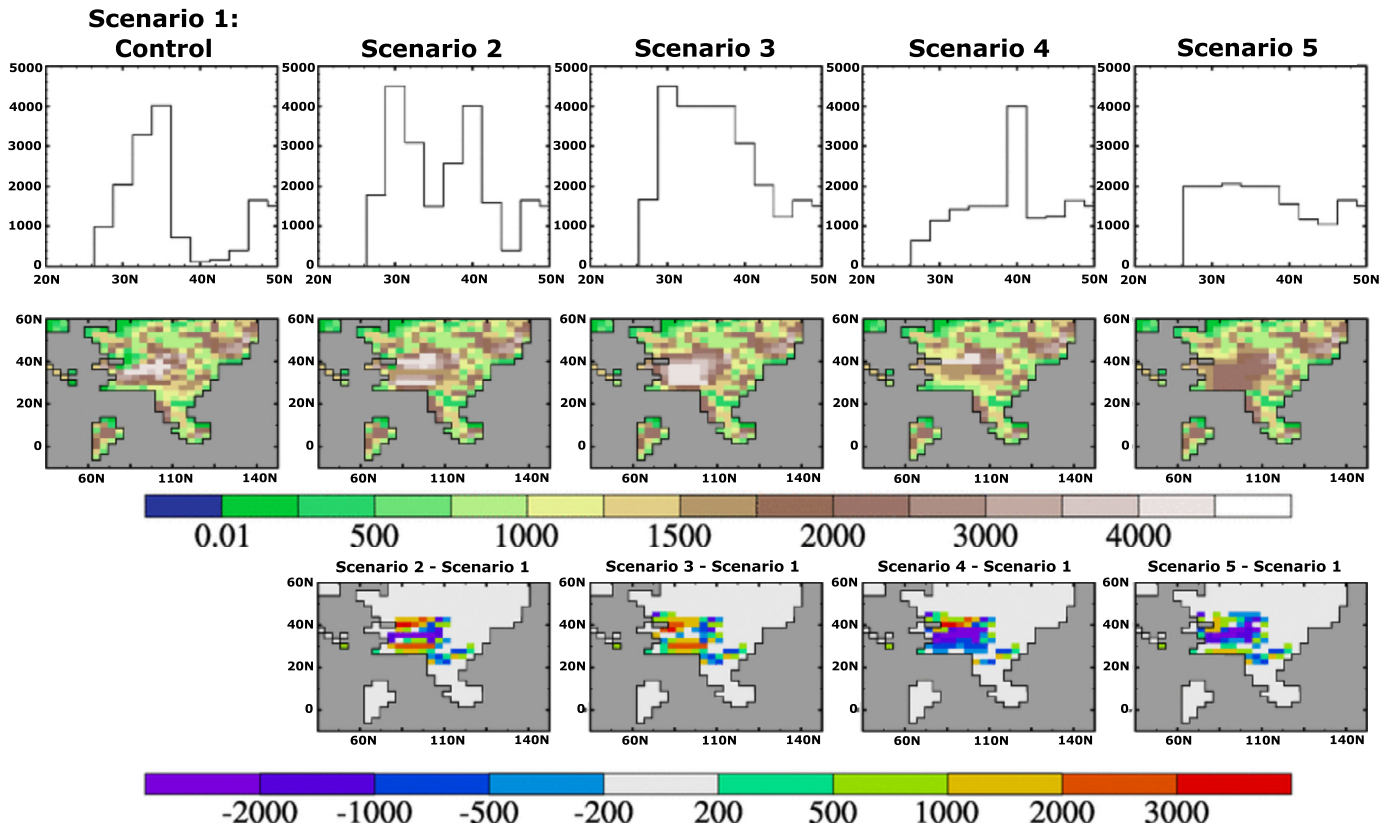

Fig. 2. Orographic reconstructions for the "control" (left column) and the 4 sensitivity simulations. The central row shows the elevations (at model resolution) for the alternative palaeoelevation of Tibet. Contours represent topographic height (m). The bottom row shows the difference between each scenario and scenario 1 (the "control") topographic height (m; contours represent the relative topographic height change). The top row shows a cross-section at 80°E, illustrating the different behaviours of each terrane for each scenario. All plots show the resolution of the input files to the GCM.

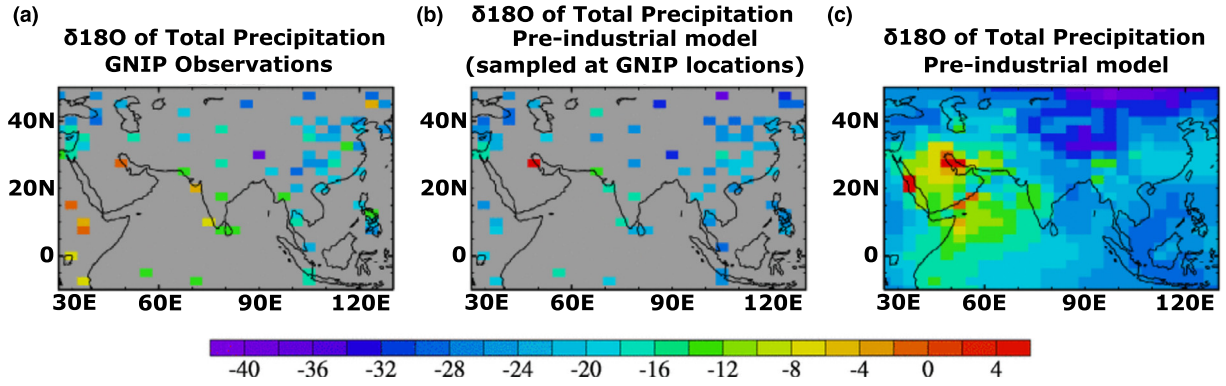

Fig. 3. Comparison of GNIP modern observations compared to a pre-industrial simulation of HadCM3L. All results are for the precipitation weighted δ^{18}O annual mean for (a) GNIP modern observations, (b) Pre-industrial HadCM3L simulation, sampled at the locations of the observations, and (c) Pre-industrial HadCM3L simulation.

GNIP reporting period for Lhasa was 1986–1992. This period coincided with a strong El Niño (1986-87, 1987-88) and strong La Niña event (1988-1989). Cai et al. (2017) had shown a positive isotope-El Niño Southern Oscillation (ENSO) response. El Niño events lead to a positive anomaly on δ^{18}O values and La Niña events lead to a negative anomaly on δ^{18}O values. Furthermore, isotopic anomalies tend to be amplified during La Niña events compared with El Niño. This signal is amplified with increasing height impacting sites like Lhasa more than low laying sites like New Delhi (where we show better agreement; Fig. 4). The strong La Nina event and high elevation may be biasing the Lhasa site to more depleted values. Similar strongly negative δ^{18}O values are also shown by (Tian et al., 2007), who sampled in Lhasa between September 1998-2001, a period that also experienced a strong La Niña event (1998-2001). This highlights the challenges and need for long-term (several decades) reporting of δ^{18}O and δD to allow for more robust comparison and evaluation of isotope-enabled climate models.

We then examined the modelled δ^{18}O-based elevation lapse rate for the pre-industrial simulation. Ideally, isotope palaeoaltimetry calculates elevation based on the difference between the δ^{18}O value at the elevated site minus the δ^{18}O value at a sea-level site at the start of a given air parcel journey. In practice, the exact source will not be known so normally the difference is taken using an average value to the south of the Himalaya. We therefore calculate $\Delta(\delta^{18}O)$, where the difference is computed from the average δ^{18}O of precipitation over the eastern Arabian sea (10°N-20°N, 60°E-80°E), broadly representing the source of summer monsoon water to the Tibetan region. In our isotope-enabled General Cir-

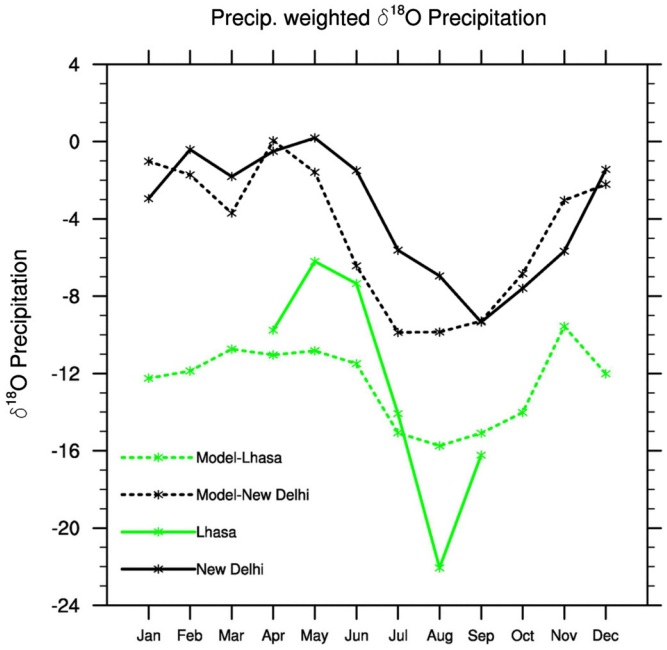

Fig. 4. Seasonal cycle of precipitation weighted $\delta^{18}O$ from GNIP observations and pre-industrial model simulations for New Delhi (black lines) and Lhasa (green lines).

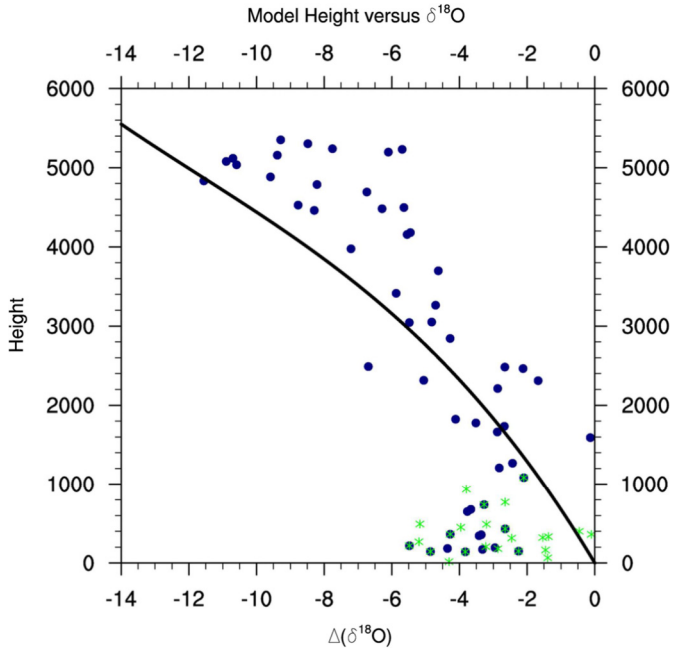

Fig. 5. For modern-day conditions, scatter plot of elevation versus June-July-Aug-Sep $\delta^{18}O$ in precipitation for all model land points in the domain (blue symbols) 10°N to 40°N, 70°E-100°E (green symbols show points from 10°N to 25°N). The changes are relative to the mean value of marine precipitation in the Eastern Arabian sea (10°N-20°N, 60°E-80°E). Also shown is the theoretical curve for the weighted mean simple Rayleigh fractionation using a range of possible temperatures and relative humidity (from Rowley, 2007).

culation Model (GCM), this works out as $-5.0‰$ which is similar to the $-6.0 \pm 1.6‰$ used by Rowley and Currie (2006) and the observed value for New Delhi ($-5.8‰$).

We then examined the relationship between summer (June-July-Aug-Sep) precipitation and $\delta^{18}O$ values (Fig. 5) of precipitation for all model land points in the domain 10°N to 40°N, 70°E to 100°E (green symbols show points from 10°N to 25°N). Also shown is the theoretical curve for Rayleigh fractionation using a surface temperature of 299 K and relative humidity of 80% (Rowley, 2007). Low elevation sites show considerable variability and do not follow any clear relationship with elevation. This is not surprising. Most of the low elevation sites are south of the Himalaya and simply show the "precipitation amount" effect (Moore et al., 2014), namely that the oxygen isotopes in meteoric water become more depleted the more that it rains. This happens as maritime air penetrates the Indian continent (and associated land atmosphere-surface-vegetation interactions), highlighting how important it is to select the baseline depleted in $\delta^{18}O$ and δD values near the region where ascent begins. With decreasing large-scale stratiform rainfall and increasing convective precipitation, the influence of the amount effect will decrease.

Further north and below about 3 km elevation, the agreement with the simple theoretical curve is relatively good, with an average scatter of about 800 m between maximum and minimum

height for any given $\delta^{18}O$ value. However, at higher elevations, the model simulated $\delta^{18}O$ values become biased towards less $\delta^{18}O$ depletion compared to Rayleigh fractionation-based oxygen isotope palaeoaltimetry theory. This bias is consistent with the fact that convective precipitation shows less fractionation at higher elevation than the large-scale precipitation that is assumed in the simple Rayleigh fractionation theory (Rowley, 2007). This arises because of differences in ice formation, growth, and melting between convective and stratiform clouds, resulting in different $\delta^{18}O$ values in meteoric water (Aggarwal et al., 2016). Thus, with decreasing concentrations of large-scale (stratiform) and increasing concentrations of convective precipitation fractional influences, the amount effect will decrease. Observational studies suggest an alternative possibility with the North of the plateau being influenced by different moisture source(s) as well as the addition of recycled surface waters and sub-cloud evaporation (Bershaw et al., 2012; Li and Garzione, 2017; Tian et al., 2007; Yao et al., 2013).

Similarly, the scatter around the black theoretical curve (Fig. 5) is likely related to the numerous other assumptions within it. For instance, the simple theory (which is based on following a parcel of air during ascent over the orography) should be applied to the difference between the $\delta^{18}O$ values at elevation and the maritime source region as well as immediately prior to any ascent. Although we could calculate this within the model, it is never possible to do this from observations. In all applications of isotope altimetry, a generic value is used, frequently based on typical modern values at sea level or at a single location such as New Delhi. Such an assumption is necessarily crude and is likely to produce major scatter in the overall relationship. For instance, Fig. 3c shows that there can be more than 3‰ variation at 25°N on the southern flanks of the Himalaya and this would, depending on the precise source of the air parcel ascent, change the palaeoelevation estimate by more than 1000 m.

Further evaluation of the isotope model for the Pre-industrial has been undertaken using a site-specific model-data comparison (Table 1). Here, we geo-locate 41 $\delta^{18}O$ samples (Bershaw et al., 2012; Li and Garzione, 2017; Tian et al., 2007; Yao et al., 2013) locations through the Tibetan plateau and surrounding regions to their equivalent model grid-point location. In general, where topographic height between the model location and the observation location are equivalent (within a range of ±750 m) there is agreement in the $\delta^{18}O$ signal (e.g. Sites Modoi, Gaize, Hetian, Lanzhou, Chengdu; Table 1). However, there are some sites where there is a lack of agreement, for example Baidi and Dui, where there is a 4.6‰ and 4.5‰ difference respectively between the model and observations. Both sites are high elevation sites with generally lower surrounding model topographic heights than reality at this resolution. This is potentially biasing the model $\delta^{18}O$ towards lower values, highlighting the importance of going to higher spatial resolutions that better resolve local topographic features when undertaking local comparison.

Unfortunately, it is challenging to make a robust like-for-like comparison between the model and observations. This is result of i) resolution dependencies. Low-resolution (∼100-300 km) isotope-enabled climate models have topographies that are not representative of local scale features (e.g. mountain tops, small basins and deeply incised river valleys) for many observation locations (see Table 1). ii) There is potential for an emergent anthropogenic signal within the observed $\delta^{18}O$ values due to high altitude regions being more sensitive, which will not be present within our Pre-industrial setup. iii) There is significant variability in $\delta^{18}O$ observations. Tian et al. (2007) show an annualised $\delta^{18}O$ signal of −12.6‰, less than that of Yao et al. (2013) who report an annualised $\delta^{18}O$ signal of −16.2‰. Different studies and observation networks will often have different reporting periods. Some studies can range from several months during the summer of one year (even assuming an annualised signal due to a monsoonal climate (Tian et al., 2007)) to larger more focused multi-decadal reporting as part of the GNIP database. This means some studies may be reporting a $\delta^{18}O$ 'weather' signal rather than a climatological mean, further complicating comparison between models and observations. A long-term climatological study between high-resolution isotope enabled models and observation stations throughout Tibet covering the same observation period with high-frequency sampling throughout the year would be highly beneficial for future studies undertaken by both the isotope and modelling communities.

4. Results - mid-Eocene "control" simulation

Overall, the mid-Eocene simulation (scenario 1) is similar to that published in Tindall et al. (2010) for the early Eocene except that our mid-Eocene model is somewhat cooler due to the lower CO_2 in our simulations. Nevertheless, our simulation is significantly warmer (7.8 °C) and wetter (14% increase) than the pre-industrial. This generally warmer climate results in an intensified hydrological cycle with a correspondingly strong increase in evaporation.

In the Asia region (Fig. 6), the model simulates a complex pattern of change. A palaeo-monsoon (as measured by precipitation seasonality and wind reversal, see Farnsworth et al., 2019) is present over the eastern side of the continent. The elevation is relatively low in this region, set at a maximum of 1500 m. Hence the centre of the monsoon is not coincident with the main region of high elevation of Tibet. By contrast, around Tibet the seasonality is variable. On the north-western side of the Asian continent, the dominant precipitation season is December – January (DJF). However, over Tibet itself, the precipitation has much smaller seasonality, with the southern flank exhibiting a slight dominance of June – August (JJA) precipitation.

Similarly, the annual mean surface winds (Fig. 6e) show a complicated structure in their seasonality (not shown). In DJF, the flow is generally westerly or south-westerly whereas in summer there is a difference between the northern and southern flanks of Tibet: there are northerlies on the northern side of Tibet, and southerlies on the southern flanks. These patterns are also broadly seen at lower tropospheric levels (850 hPa), but the winds are relatively weak at this level in DJF (at 500 hPa the westerlies are strong).

This complex seasonality in precipitation and winds raises interesting challenges in understanding the selection of the low-level source of the moisture precipitation on Tibet. On the southern flanks of Tibet, the winds would suggest that the moisture is sourced from the south and hence successful application of isotope altimetry would imply seeking terrestrial oxygen isotope proxies at near-sea level in this region. These values can be estimated from the model and are driven strongly by those in the surface of the adjacent ocean. The surface ocean temperatures are warm with a significant area above 27 °C and reaching above 29 °C at 20°N, 90°E. This, combined with the downwelling part of the Hadley Cell at 20°N (as shown by the near-zero precipitation) and the strong low-level flow, results in a strongly evaporative ocean, high surface salinity (not shown), and a surface ocean enriched in $\delta^{18}O$ and δD (Fig. 6f). This is then reflected in the $\delta^{18}O$ values of precipitation, which are also relatively enriched along the northern coast of the shallow seaway between India and Asia. We calculated the weighted $\delta^{18}O$ of precipitation for all land data points below 500 m in the region from 70°E-100°E, 20°N-25°N, resulting in a weighted mean average of −3.4‰ for JJA and −4.7‰ for the annual mean. If we instead assume that in DJF (and in the annual mean) the source is more from the west than from the south, then the annual mean $\delta^{18}O$ values are −4.5‰.

Table 1
Model-data comparison of $\delta^{18}O$ values in Tibet and neighbouring regions. D = $\delta^{18}O$ observation location. M = $\delta^{18}O$ model location.

Data source	Station name	Latitude (°N)	Longitude (°E)	Altitude (m)	Annual $\delta^{18}O$ of precipitation (‰), VSMOW	JJA $\delta^{18}O$ of precipitation (‰), VSMOW	DJF $\delta^{18}O$ of precipitation (‰), VSMOW	Reference
D	Nyalam 1	85°58′E	28°11′N	3810	-10.7	-15.1	-10.0	Tian et al., 2007
M		82.5E	30N	4692	-9.2	-8.4	-10.8	-
D	Lhasa 1	91°02′E	29°43′N	3658	-12.6	-17.4	-	Tian et al., 2007
M		90E	30N	4883	-11.1	-11.3	-11.9	-
D	Shiquanhe 1	80°06′E	32°30′N	4280	-14.0	-11.4	-	Tian et al., 2007
M		78.75E	32.5N	4481	-9.6	-8.5	-11.3	-
D	Gaize 1	84°03′E	32°18′N	4420	-13.0	-9.8	-13.9	Tian et al., 2007
M		86.25N	32.5N	5119	-11.4	-10.6	-16.3	-
D	JBTB-01	100.0424E	37.1993N	2216	-	-7.8	-	Bershaw et al., 2012
M		101.25E	37.5N	3176	-9.5	-9.2	-12.6	-
D	JBTB-25	97.7523E	33.4954N	3394	-	-13.7	-	Bershaw et al., 2012
M		97.5E	35.0N	4528	-10.6	-9.8	-17.0	-
D	JBTB-29	91.6872	34.4763	3529	-	-11.9	-	Bershaw et al., 2012
M		90E	35.0N	5303	-10.4	-8.8	-20.4	-
D	JBTB-39	96.4192E	32.3663N	3678	-	-14.4	-	Bershaw et al., 2012
M		97.5E	32.5N	4833	-12.0	-12.0	-13.7	-
D	JBTB-46	97.2953E	31.0201N	3175	-	-15.4	-	Bershaw et al., 2012
M		97.5E	30N	4461	-9.3	11.0	-8.3	-
D	Zhangmu	85°59′E	27°59′N	2239	-	-13.2	-	Yao et al., 2013
M		86.25N	27.5N	2482	-8.8	-8.5	-6.9	-
D	Nylam 2	85°58′E	28°11′N	3810	-12.4	-14.7	-10.8	Yao et al., 2013
M		86.25N	27.5N	2482	-8.8	-8.5	-6.9	-
D	Dui	90°32′E	28°35′N	5030	-18.6	-19.0	-6.8	Yao et al., 2013
M		90E	27.5N	2843	-8.6	-9.2	-6.6	-
D	Dingri	87°07′E	28°39′N	4330	-18.1	-18.2	-15.4	Yao et al., 2013
M		86.25E	27.5N	2482	-8.5	-8.8	-6.9	-
D	Wnegguo	90°21′E	28°54′N	4500	-16.5	-17.6	-	Yao et al., 2013
M		90E	27.5N	2843	-8.6	-9.2	-6.6	-
D	Larzi	87°41′E	29°05′N	4000	-20.3	-	-	Yao et al., 2013
M		90E	27.5N	2843	-8.6	-9.2	-6.6	-
D	Baidi	90°26′E	29°07′N	4430	-15.7	-17.1	-17.2	Yao et al., 2013
M		90E	30N	4883	-11.1	-11.3	-11.9	-
D	Nuxia	94°34′E	29°28′N	2780	-	-18.3	-	Yao et al., 2013
M		93.75E	30N	4497	-7.8	-9.7	-7.8	-
D	Lhasa 2	91°08′E	29°42′N	3658	-16.2	-17.3	-11.7	Yao et al., 2013
M		90E	30N	4883	-11.1	-11.3	-11.9	-
D	Lulang	94°44′E	29°46′N	3327	-14.5	-14.7	-19.1	Yao et al., 2013
M		93.75E	30N	4497	-7.8	-9.7	-7.8	-
D	Bomi	95°46′E	29°52′N	2737	-11.8	-14.0	-13.3	Yao et al., 2013
M		93.75E	30N	4497	-7.8	-9.7	-7.8	-
D	Yangcum	91°53′E	29°53′N	3500	-15.9	-18.2	-	Yao et al., 2013
M		90E	30N	4883	-11.1	-11.3	-11.9	-
D	Nagqu	92°04′E	31°29′N	4508	-16.5	-17.0	-17.8	Yao et al., 2013
M		93.75E	32.5N	5036	-11.4	-11.3	-14.0	-
D	Gaize 2	84°04′E	32°18′N	4430	-12.3	-10.6	-17.4	Yao et al., 2013
M		86.25N	32.5N	5119	-11.4	-10.6	-16.3	-
D	Shiquanhe 2	80°05′E	32°30′N	4278	-14.4	-14.3	-18.8	Yao et al., 2013
M		78.75E	32.5N	4481	-9.6	-8.5	-11.3	-
D	Yushu	97°01′E	33°01′N	3682	-13.1	-13.2	-15.7	Yao et al., 2013
M		97.5E	35.0N	4528	-10.6	-9.8	-17.0	-
D	Tuotuohe	92°26′E	34°13′N	4533	-11.9	-10.9	-21.6	Yao et al., 2013
M		93.75E	35.0N	4787	-10.5	-9.5	-14.8	-
D	Kabul	69°05′E	34°40′N	1860	-7.2	0.4	-10.5	Yao et al., 2013
M		67.5N	35.0N	2709	-9.2	-5.0	-10.2	-

(*continued on next page*)

Table 1 (*continued*)

Data source	Station name	Latitude (°N)	Longitude (°E)	Altitude (m)	Annual $\delta^{18}O$ of precipitation (‰), VSMOW	JJA $\delta^{18}O$ of precipitation (‰), VSMOW	DJF $\delta^{18}O$ of precipitation (‰), VSMOW	Reference
D	Lanzhou 1	103°51′E	36°03′N	1517	-5.6	-4.6	-13.0	Yao et al., 2013
M		105.0E	35.0N	2096	-7.8	-8.5	-7.6	-
D	Hetian	79°34′E	37°05′N	1375	-5.5	-2.2	-17.8	Yao et al., 2013
M		78.75E	37.5N	2211	-7.8	-6.3	-15.4	-
D	Delingha	97°22′E	37°22′N	2981	-7.7	-6.3	-19.9	Yao et al., 2013
M		97.5E	37.5N	3976	-11.6	-9.1	-19.5	-
D	Taxkorgen	75°16′E	37°46′N	3100	-6.8	-3.1	-21.0	Yao et al., 2013
M		75.0E	37.5N	4156	-12.3	-7.4	-17.5	-
D	Zhangye 1	100°26′E	38°56′N	1483	-6.0	-4.3	-18.7	Yao et al., 2013
M		101.25E	37.5N	3176	-9.5	-9.2	-12.6	-
D	Urumqi	87°36′E	43°48′N	918	-10.8	-6.3	-20.6	Yao et al., 2013
M		86.25N	42.5N	2083	-11.7	-7.6	-19.9	-
D	Modoi	98.26E	34.92N	4300	-12.2	-	-	Li and Garzione, 2017
M		97.5E	35.0N	4528	-10.6	-9.8	-17.0	-
D	Wolong	102.97E	30.86N	2805	-11.7	-	-	Li and Garzione, 2017
M		101.25E	30N	3593	-8.8	-10.7	-3.6	-
D	Lanzhou 2	103.85E	36.05N	1517	-7.1	-	-	Li and Garzione, 2017
M		105.0E	35.0N	2096	-7.8	-8.5	-7.6	-
D	Lanzhou 2	103.85E	36.05N	1517	-7.1	-	-	Li and Garzione, 2017
M		105.0E	35.0N	2096	-7.8	-8.5	-7.6	-
D	Dui	90.53E	28.58N	5030	-18.6	-	-	Li and Garzione, 2017
M		90E	30N	4883	-11.1	-11.3	-11.9	-
D	Zhangye 2	100°26′E	38°56′N	1483	-6.6	-	-	Li and Garzione, 2017
M		101.25E	37.5N	3176	-9.5	-9.2	-12.6	-
D	Xining	101.77E	36.62N	2261	-6.8	-	-	Li and Garzione, 2017
M		101.25E	37.5N	3176	-9.5	-9.2	-12.6	-
D	Chengdu	104.02E	30.67N	506	-7.1	-	-	Li and Garzione, 2017
M		105.0E	30N	557	-7.2	-9.6	-1.8	-

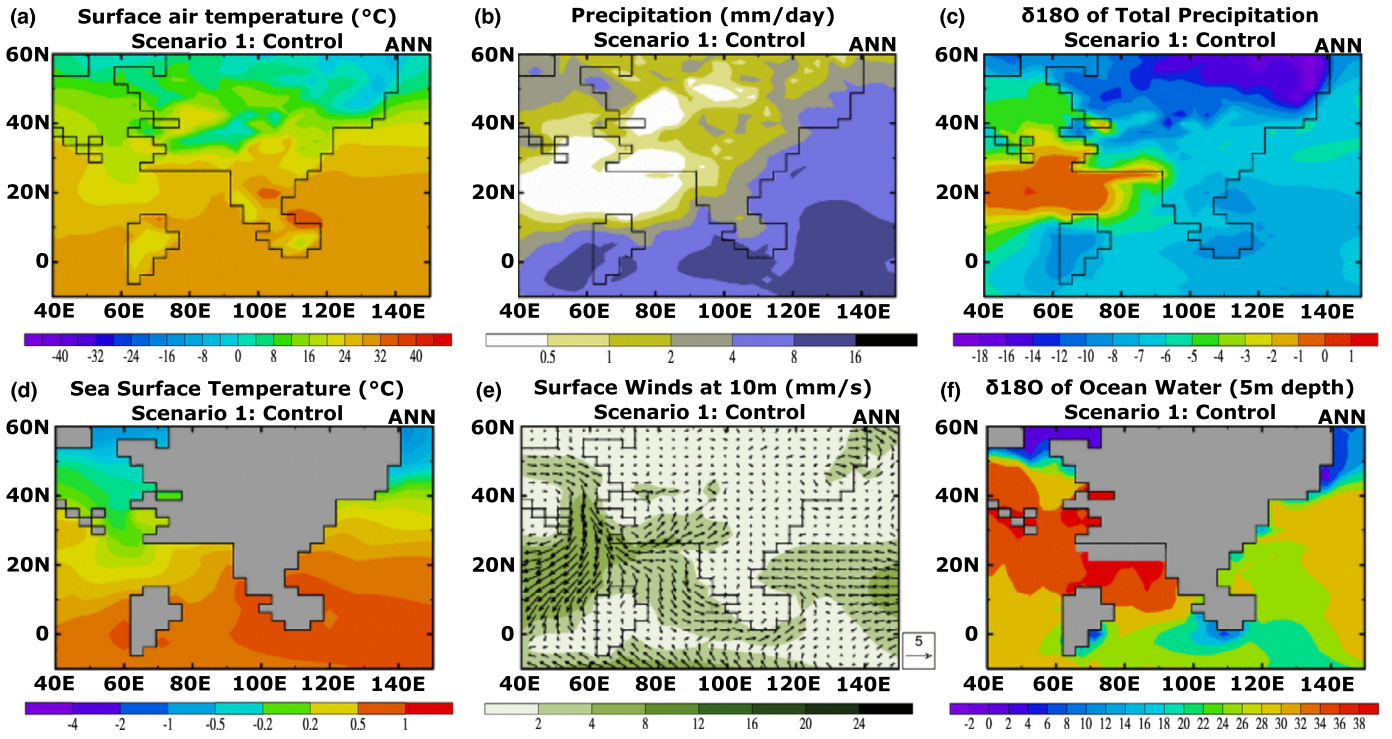

Fig. 6. Simulation results for scenario 1 (the "control") for the annual mean, showing (a) Surface Air Temperature (in °C), (b) Total Precipitation (in mm/day), (c) $\delta^{18}O$ values of precipitation (in ‰), (d) Sea Surface Temperature (in °C), (e) Surface (10 m) wind strengths and directions (in m/s with the inset showing the length of the 5 m/s vector), and (f) Sea surface $\delta^{18}O$ values (in ‰).

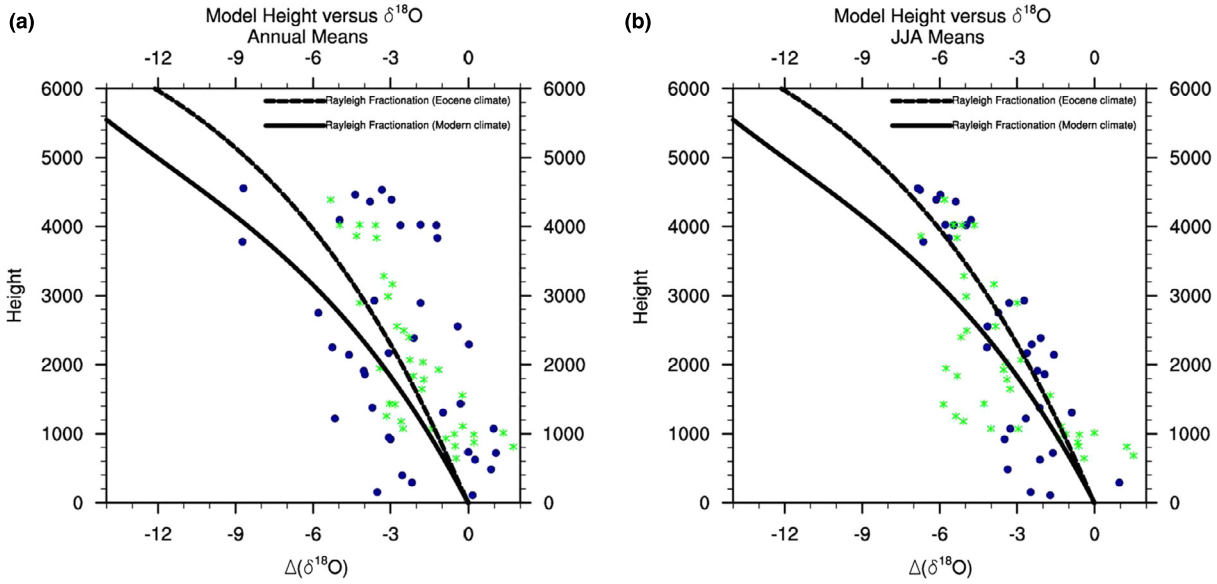

Fig. 7. For the mid-Eocene, scatter plot of elevation versus (a) Annual mean, and (b) June-July-August $\delta^{18}O$ in precipitation for all model land points (blue symbols) in the domain 20°N to 45°N, 70°E-100°E (green symbols show points from 10°N to 35°N). The changes are relative to the estimated mean value of the source region (see text). Also shown is the theoretical curve for the weighted mean simple Rayleigh fractionation using a range of possible temperatures and relative humidity (from Rowley (2007)) for the modern (solid line), and the early Eocene (dashed line).

For the following discussion, we selected the *southern* source value for JJA and the western source value for annual means. For the northern flanks of Tibet, a similar situation applies with the exception of some offsets, such as in the ocean to the northwest of Tibet, the $\delta^{18}O$ of surface ocean water is generally considerably reduced in relation to that to the south (Fig. 6f). However, in our palaeogeographic reconstruction, there is an enclosed seaway (two ocean grid boxes) where there is no flow to the Para-Tethys. The ocean $\delta^{18}O$ values in this enclosed seaway are high (enriched), and this is also reflected in high isotopic values for the precipitation in this region. This potentially has an impact on the $\delta^{18}O$ of the source region. We calculated the weighted $\delta^{18}O$ of precipitation for all land points below 500 m in the region 70°E-100°E, 40°N-45°N, which yielded values of $-2.0‰$ and $-7.7‰$ for JJA and Annual means respectively. However, if we assume that the source is from the west, the values are $-2.5‰$ and $-6.9‰$ respectively.

We then selected the *northern* source value for JJA and the western source value for annual means. Fig. 7 uses these source region values to calculate the $\delta^{18}O$ lapse rate for JJA and annual means for data to the south of 25°N (defined as the southern flank of the Himalaya) and those north of 25°N. Also shown are simple Rayleigh fractionation lapse rate curves using typical modern temperatures (299 K) and relative humidity (80%) and the same for the warmer conditions for the mid-Eocene (Rowley, 2007). For JJA (Fig. 7b), the results from modelling and Rayleigh fractionation show remarkable consistency. Both the northern and southern flanks of the Himalaya follow the simple theory with relatively little scatter. This implies that oxygen isotope palaeoaltimetry would work remarkably well in southern Tibet if, and only if, it was possible to accurately estimate from the proxy record JJA $\delta^{18}O$ of precipitation for both the elevated site and the appropriate source region.

If we more realistically (given that the precipitation is not strongly seasonal) assume that proxy estimates reflect the annual mean conditions, then there are still encouraging results (Fig. 7a). Again, both the northern and southern sides of Tibet approximate the theoretical curve, although with more scatter. Both show a bias towards lower $\delta^{18}O$ values, indicating that our estimate of the source region $\delta^{18}O$ values were too low (depleted) by about 3‰, but this is well within the range of modern values seen in the region.

A full analysis of the source region would require an analysis at every grid point of the trajectory of air parcels at the time of precipitation. This would be possible within the model but would never be useable in a true palaeoclimate setting, and thus estimating the true source region will always be approximate and hence introduces a typical error of 3-4‰. This source of uncertainty alone equates to more than 1000 m range in elevation estimates. New methods and techniques to identify the source values will be imperative to increasing precision in isotope fractionation based paleoaltimetry studies.

5. Results - sensitivity analysis

The discussion above (Section 4) has focussed on estimating the overall palaeoelevation of the Tibetan region. We are also interested to examine whether oxygen isotope palaeoaltimetry can estimate smaller changes such as the presence of a valley system (Su et al., 2019) or the rise of one particular part of what is now the plateau. This is important given that Tibet is composed of several accreted terranes, each with its own elevation history (Rowley and Currie, 2006; Spicer et al., 2021b; Xiong et al., 2020).

To investigate this, we conducted four further simulations (see Methods) where we changed different parts of Tibetan surface height. We have focused on western Asia to emphasise the direct response of the model to the changed orography. Fig. 8 shows the changes in orography, annual mean precipitation, and annual mean $\delta^{18}O$ in precipitation for the four different scenarios relative to the "control" (scenario 1) orography. For the total precipitation, there are also some small statistically significant changes beyond the local region caused by changes to the atmospheric (and ocean) circulation. However, this is not the subject of the analysis and will not be discussed further here. For $\delta^{18}O$, the statistically significant changes are exclusively focused on the selected region.

Scenario 4 is the simplest change to the control orography, constituting an increase in elevation to the north and a decrease to the south. The response of precipitation and $\delta^{18}O$ is also straightforward. The changes in elevation produce enhanced orographic precipitation on the northern side of Tibet and reduced precipita-

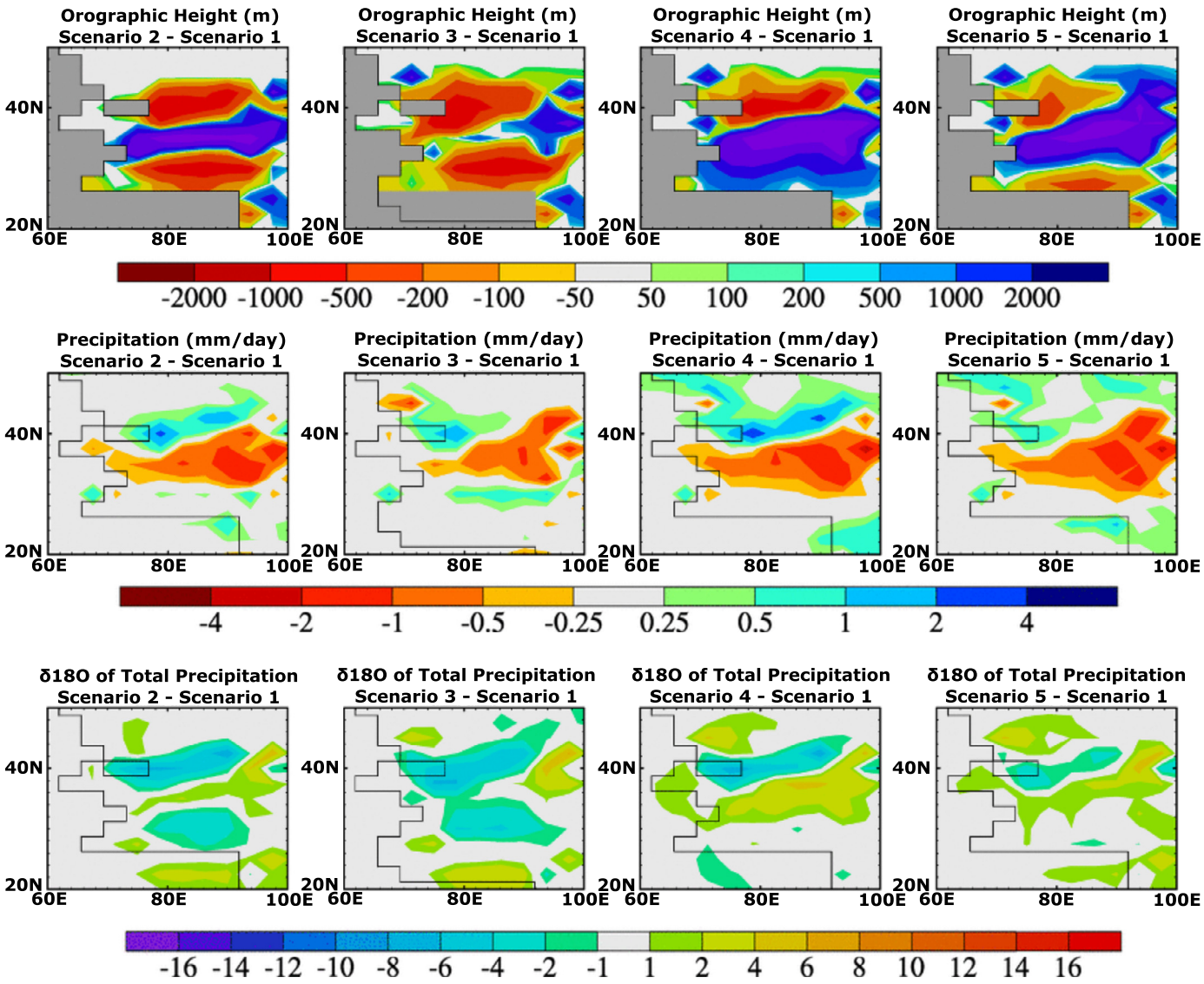

Fig. 8. Results for the four sensitivity simulations are described in the methods section. The top row shows the changes in surface elevation, relative to the "control" simulation (scenario 1). The middle row shows the changes in annual mean precipitation (in mm/day) and the lower row shows the corresponding changes in $\delta^{18}O$ in precipitation (in ‰). The left column shows scenario 2, and successively for the other scenarios. The region shown is focused on the area of elevation change in order to better visualise the changes.

tion to the south. The same pattern applies in all four seasons (not shown), but the largest increase on the northern side occurs in winter whereas the greatest decrease to the south occurs in summer.

The $\delta^{18}O$ signal follows a similar pattern in the annual mean precipitation with a decrease over the higher elevations and an increase over the lower elevation relative to scenario 1. Inspection of the seasonal $\delta^{18}O$ signals (not shown) reveals that the pattern of change is consistent throughout the year, but the biggest changes occur in the winter season for both north and south changes. These changes map well onto palaeoaltimetry theory, and a plot of change in height versus change in $\delta^{18}O$ (Fig. 9) shows the average slope for this simulation is -489 m/‰ with a standard error of the slope of 40 m/‰, similar to what Quade et al. (2011) estimated along the modern Himalaya front (-2.8‰/1000 m).

Scenario 2 has the Gangdese mountains further south than the control at about 4500 m high, and the Qiangtang mountains at 4000 m. In between the mountains is a valley system with a floor set at 1500 m. The precipitation response to these changes is very similar to scenario 4. There is an increase in orographic precipitation to the north and a decrease to the south. There is a hint of a further increase at the southern margin, but in the annual mean it is small. Further inspection of the seasonal changes (not shown) reveals that in winter the Qiangtang mountains are effectively blocking the flow of moisture to the south and hence there is a very widespread drying across the whole region south of the Qiangtang. In the summer months (JJA), there is airflow from the south and hence there is a noticeable increase in precipitation along the southern flanks of the Gangdese and a decrease further north. The valley system between the mountains experiences a decrease in precipitation throughout the year. Effectively, the valley is always in the rain shadow of either the Gangdese or Qiangtang mountains, and hence the decrease in precipitation over the valley system is much greater than either of the increases to the North or South. However, the valley bottom will still be fed from water drainage from precipitation higher up on the flanks of the Gangdese and Qiangtang.

The $\delta^{18}O$ values show similar trends to the precipitation trends, but the relative magnitudes of the high-low-high pattern is different. The inclusion of the valley has an appreciable impact on the

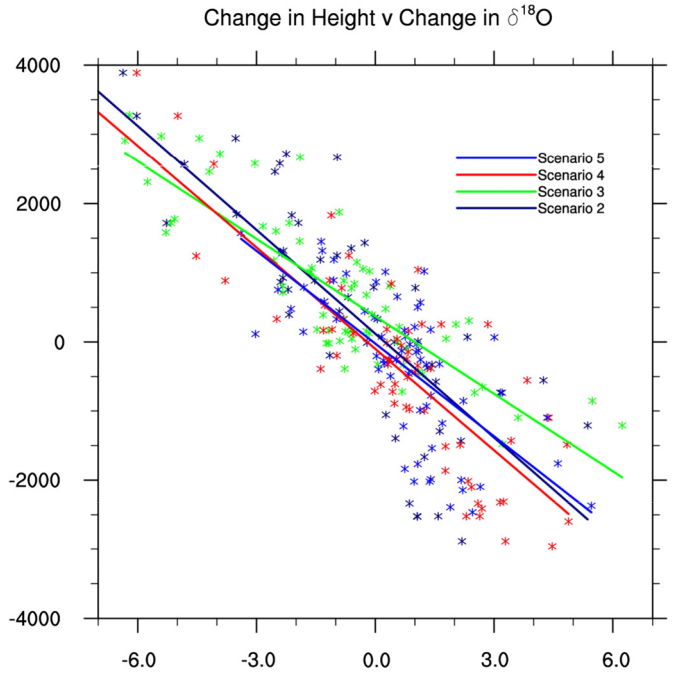

Fig. 9. Shows the relationship between the model changes in surface elevation and the change in the annual mean δ^{18}O of the precipitation. This is for all land points where the elevation has changed in the region 65°E-100°E, 25°N-50°N. The symbols show each individual grid point and the lines show the best-fit regression line.

climate of central Tibet with a marked drying (Fig. 8). However, the variation for δ^{18}O signal in the valley is much weaker than either of the signals to North or South. The δ^{18}O values become depleted as the meteoric water in the source air rises up a mountain slope but remains constant once it has reached a maximum depletion. The δ^{18}O value of precipitation decreases, but once the air reaches the summit, any further change is minimal. Thus, in winter, the largest changes are to the North; the precipitation becomes more isotopically depleted but once the air reaches the summit, there is little further depletion. Similarly, in the summer, the same process operates but with more source air rising from the South. Thus, the resulting annual mean signal better represents the increases in orography of the bounding mountain ranges but underrepresents the presence of the low valley between them. This phenomenon can result in a 'phantom' plateau where within-valley isotope signatures reflect the crest heights of the bounding mountain systems and not the elevation of the valley floor (Spicer et al., 2021b).

Examining the height versus δ^{18}O signal (Fig. 9) shows that the isotope lapse rate is relatively similar to scenario 4 (slope $= -500$ m/‰), but that the standard error is larger (55 m/‰). Examination of the underlying scatter plots shows that data points within the valley system (the region which experiences negative height changes compared to the "control", scenario 1) are consistently below the regression line, reinforcing the message that the δ^{18}O value is lower than expected for the actual elevation.

Given these two sensitivity studies (2 & 4), the results for the other two scenarios follow a broadly similar story. Scenario 3 is like scenario 2 but the valley system is no longer present. The corresponding precipitation signal is similar to scenario 2, namely the higher mountains to the north and south have enhanced precipitation on their windward sides but, in between, the system is permanently in a rain-shadow and hence rainfall is decreased. The δ^{18}O signal in scenario 3 is also near-identical to scenario 2, further emphasising that the isotope palaeoaltimetry is not able to resolve topographic detail within an otherwise high terrane. The slope and standard error are -375 m/‰ and 29 m/‰, respectively, in the valley system. The reduced value is largely because there are considerably fewer points that correspond to lower elevations and hence the best-fit regression line is not being influenced by presence of the valley system.

Finally, scenario 5 consists of a flatter, low plateau orography. Surface elevations are near-constant at 2000 m from 25°N to 40°N. Compared to scenario 1, this implies an increase in the height of the central region of Tibet while there is a decrease in the south (Fig. 8; top row). This then still results in a tri-pole pattern of precipitation and the δ^{18}O values change, but with slightly smaller amplitudes for the peaks and troughs. The slope and standard error are -447 m/‰ and 59 m/‰ respectively. The reduction in maximum heights to the north and south means that the central plateau does not experience as strong a rain shadow, but overall the patterns are the same.

6. Conclusions

Most previous isotope-enabled modelling studies examining Tibetan Plateau formation and palaeoaltimetry have used present-day boundary conditions to perform simulations. Our study has focussed on simulations using more realistic mid-Eocene boundary conditions and a suite of possible orographies for what is now the Tibetan plateau region. The results have broadly shown that the isotope system does follow the simple Rayleigh fractionation curves of Rowley (2007), Rowley and Currie (2006), DeCelles et al. (2007), etc., especially in southern Tibet, but with considerable scatter around the line (with typical errors up to 1000 m) and even larger scatter at lower elevations.

We find:

- Accuracy in following the simple Rayleigh fractionation curves is improved when picking an appropriate mean sea level source of meteoric water and its δ^{18}O values. Depending on the airflow direction and season of maximum precipitation, there can be more than a 3‰ difference, which equates to more than 1000 m change in a palaeoelevation estimates (similar to that of using inappropriate dry-bulb lapse rates (Farnsworth et al., 2021)). Failure to do so may have led to previous studies quoting inaccurate elevations and/or underestimating uncertainty.
- There is a strong correlation between elevation change and δ^{18}O changes against single mountain barriers with a prevailing wind system, with the expected exception that the method cannot resolve valley systems within otherwise high orography. This means Tibet will always appear as a plateau irrespective of the true topographic complexity.
- Small changes in elevation have also been shown to accurately follow Rayleigh fractionation curves. This is because small changes in elevation do not cause major changes to the circulation or humidity fields, with the response being simply isotopic depletion as the air parcel rises over the topography.
- Due to the importance that palaeo-specific boundary conditions play in ocean and atmospheric circulation, it is inappropriate to use models with modern/highly dissimilar boundary conditions to the time period being investigated.
- Our study has not considered other sources of uncertainties. Our palaeogeographic reconstructions do not include any lakes within the Tibet region so there is no recycling of lacustrine moisture, with the exception of soil evaporation. However, the isotopic composition of such lakes would likely resemble the overall isotopic signal, rather than fundamentally modifying it. We have also not included any analysis of potential issues associated with the correlation between δ^{18}O of precipitation and the δ^{18}O of the carbonate from which isotopic signals are extracted. Both can lead to significant further sources of error and uncertainty (Xiong et al., 2022).

- It is also unclear how model-dependent these results are. Future work incorporating a more detailed intercomparison of other isotope-enabled palaeoclimate models (e.g. CESMi) would help evaluate this uncertainty.
- Additionally, it is unknown how much influence spatial resolution of specific topographic features, such as a narrow valley sandwiched between two high mountains, has on the isotopic signature. We have shown even at this course model resolution climate, in particular the hydrological regime of central Tibet, is modified by the inclusion of a deep E-W aligned valley ~300 km wide in a N-S direction, yet despite the large size of the valley the isotopic signature does not reflect its presence. Employing a high spatial resolution isotope-enabled model (perhaps even approaching convective permitting scales) should be a focus of future work to explicitly determine the influence of model resolution on oxygen isotopes in complex terranes.
- Lastly, there is another source of uncertainty arising as a result of the global paleogeography chosen. Other mid-Eocene paleogeographies (with a similar inclusion of a dual mountain and wide central Tibetan valley; Scenario 2) may lead to differences in ocean and atmospheric circulation. This may also lead to changes in the mean sea level source of meteoric water and its $\delta^{18}O$ value, as well as its advection into Tibet.

Overall, we conclude that stable isotope water palaeoaltimetry is a potentially powerful tool for estimating past changes in surface elevation, but the errors associated with this method have been underestimated. These uncertainties can be reduced if used in conjunction with climate models that can better quantify both the source origin and the low elevation $\delta^{18}O$. Despite these large errors, the method works surprisingly well except it cannot resolve valley systems within an otherwise high topography.

CRediT authorship contribution statement

Alex Farnsworth: Conceptualization, Data curation, Formal analysis, Investigation, Methodology, Project administration, Writing – original draft, Writing – review & editing. **Paul J. Valdes:** Conceptualization, Formal analysis, Funding acquisition, Investigation, Project administration, Software, Writing – original draft, Writing – review & editing. **Lin Ding:** Writing – review & editing. **Robert A. Spicer:** Writing – review & editing. **Shi-Hu Li:** Writing – review & editing. **Tao Su:** Writing – review & editing. **Shufeng Li:** Writing – review & editing. **Caitlyn R. Witkowski:** Writing – review & editing. **Zhongyu Xiong:** Writing – review & editing.

Declaration of competing interest

The authors declare that they have no known competing financial interests or personal relationships that could have appeared to influence the work reported in this paper.

Data availability

Data will be made available on request.

Acknowledgements

This work is supported by the National Natural Science Foundation of China and Natural Environment Research Council of the UK joint research program (No. 41661134049 to T.S., No. NE/P013805/1 to A.F., P.J.V., and C.R.W.), and National Natural Science Foundation of China BSCTPES project (No. 41988101 to L.D.), and Second Tibetan Plateau Scientific Expedition and Research Program (grant no. 2019QZKK0708). R.A.S. is also supported by a Senior Visiting Scientist position at XTBG. A.F. also acknowledges Chinese Academy of Sciences Visiting Professorship for Senior International Scientists (Grant No. 2021FSE0001).

References

Aggarwal, P.K., Romatschke, U., Araguas-Araguas, L., Belachew, D., Longstaffe, F.J., Berg, P., Schumacher, C., Funk, A., 2016. Proportions of convective and stratiform precipitation revealed in water isotope ratios. Nat. Geosci. 9, 624–629. https://doi.org/10.1038/ngeo2739.

An, W., Hu, X., Garzanti, E., Wang, J.-G., Liu, Q., 2021. New precise dating of the India-Asia collision in the Tibetan Himalaya at 61 Ma. Geophys. Res. Lett. 48, e2020GL090641. https://doi.org/10.1029/2020GL090641.

Bershaw, J., Penny, S.M., Garzione, C.N., 2012. Stable isotopes of modern water across the Himalaya and eastern Tibetan Plateau: implications for estimates of paleoelevation and paleoclimate. J. Geophys. Res., Atmos. 117. https://doi.org/10.1029/2011JD016132.

Botsyun, S., Sepulchre, P., Donnadieu, Y., Risi, C., Licht, A., Caves Rugenstein, J.K., 2019. Revised paleoaltimetry data show low Tibetan Plateau elevation during the Eocene. Science 363, eaaq1436. https://doi.org/10.1126/science.aaq1436.

Botsyun, S., Sepulchre, P., Risi, C., Donnadieu, Y., 2016. Impacts of Tibetan Plateau uplift on atmospheric dynamics and associated precipitation $\delta^{18}O$. Clim. Past 12, 1401–1420. https://doi.org/10.5194/cp-12-1401-2016.

Brenner, A.R., Fu, R.R., Evans, D.A.D., Smirnov, A.V., Trubko, R., Rose, I.R., 2020. Paleomagnetic evidence for modern-like plate motion velocities at 3.2 Ga. Sci. Adv. 6, eaaz8670. https://doi.org/10.1126/sciadv.aaz8670.

Cai, Z., Tian, L., Bowen, G.J., 2017. ENSO variability reflected in precipitation oxygen isotopes across the Asian summer monsoon region. Earth Planet. Sci. Lett. 475, 25–33. https://doi.org/10.1016/j.epsl.2017.06.035.

Dansgaard, W., 1964. Stable isotopes in precipitation. Tellus 16, 436–468.

DeCelles, P.G., Quade, J., Kapp, P., Fan, M., Dettman, D.L., Ding, L., 2007. High and dry in central Tibet during the late oligocene. Earth Planet. Sci. Lett. 253, 389–401. https://doi.org/10.1016/j.epsl.2006.11.001.

Deng, T., Ding, L., 2015. Paleoaltimetry reconstructions of the Tibetan Plateau: progress and contradictions. Natl. Sci. Rev. 2, 417–437. https://doi.org/10.1093/nsr/nwv062.

Ding, L., Spicer, R.A., Yang, J., Xu, Q., Cai, F., Li, S., Lai, Q., Wang, H., Spicer, T.E.V., Yue, Y., Shukla, A., Srivastava, G., Khan, M.A., Bera, S., Mehrotra, R., 2017. Quantifying the rise of the Himalaya orogen and implications for the South Asian monsoon. Geology 45, 215–218. https://doi.org/10.1130/G38583.1.

Ding, L., Xu, Q., Yue, Y., Wang, H., Cai, F., Li, S., 2014. The Andean-type Gangdese mountains: paleoelevation record from the Paleocene–Eocene Linzhou basin. Earth Planet. Sci. Lett. 392, 250–264. https://doi.org/10.1016/j.epsl.2014.01.045.

Ehlers, T.A., Poulsen, C.J., 2009. Influence of Andean uplift on climate and paleoaltimetry estimates. Earth Planet. Sci. Lett. 281, 238–248. https://doi.org/10.1016/j.epsl.2009.02.026.

Farnsworth, A., Lunt, D.J., Robinson, S.A., Valdes, P.J., Roberts, W.H.G., Clift, P.D., Markwick, P., Su, T., Wrobel, N., Bragg, F., Kelland, S.-J., Pancost, R.D., 2019. Past East Asian monsoon evolution controlled by paleogeography, not CO2. Sci. Adv. 5, eaax1697. https://doi.org/10.1126/sciadv.aax1697.

Farnsworth, A., Valdes, P.J., Spicer, R.A., Ding, L., Witkowski, C., Lauretano, V., Su, T., Li, Shufeng, Li, Shihu, Zhou, Z., 2021. Paleoclimate model-derived thermal lapse rates: towards increasing precision in paleoaltimetry studies. Earth Planet. Sci. Lett. 564, 116903. https://doi.org/10.1016/j.epsl.2021.116903.

Farquhar, G.D., Cernusak, L.A., Barnes, B., 2007. Heavy water fractionation during transpiration. Plant Physiol. 143, 11–18. https://doi.org/10.1104/pp.106.093278.

Feng, R., Poulsen, C.J., Werner, M., Chamberlain, C.P., Mix, H.T., Mulch, A., 2013. Early Cenozoic evolution of topography, climate, and stable isotopes in precipitation in the North American cordillera. Am. J. Sci. 313, 613–648. https://doi.org/10.2475/07.2013.01.

Forest, C.E., Molnar, P., Emanuel, K.A., 1995. Palaeoaltimetry from energy conservation principles. Nature 374, 347–350. https://doi.org/10.1038/374347a0.

Foster, G.L., Royer, D.L., Lunt, D.J., 2017. Future climate forcing potentially without precedent in the last 420 million years. Nat. Commun. 8, 14845. https://doi.org/10.1038/ncomms14845.

Garzione, C.N., Dettman, D.L., Quade, J., DeCelles, P.G., Butler, R.F., 2000. High times on the Tibetan Plateau: paleoelevation of the Thakkhola graben. Nepal Geol. 28, 339–342. https://doi.org/10.1130/0091-7613(2000)28<339:HTOTTP>2.0.CO;2.

Global Network of Isotopes in Precipitation (GNIP), 2019. [WWW Document]. https://www.iaea.org/services/networks/gnip. (Accessed 18 February 2022).

Gregory-Wodzicki, K.M., McIntosh, W.C., Velasquez, K., 1998. Climatic and tectonic implications of the late Miocene Jakokkota flora, Bolivian Altiplano. J. South Am. Earth Sci. 11, 533–560. https://doi.org/10.1016/S0895-9811(98)00031-5.

Hoke, G.D., 2018. Geochronology transforms our view of how Tibet's southeast margin evolved. Geology 46, 95–96. https://doi.org/10.1130/focus012018.1.

Huber, M., Goldner, A., 2012. Eocene monsoons. In: Asian Clim. & Tecton. J. Asian Earth Sci. 44, 3–23. https://doi.org/10.1016/j.jseaes.2011.09.014.

Ingalls, M., Rowley, D., Olack, G., Currie, B., Li, S., Schmidt, J., Tremblay, M., Polissar, P., Shuster, D.L., Lin, D., Colman, A., 2017. Paleocene to Pliocene low-

latitude, high-elevation basins of southern Tibet: implications for tectonic models of India-Asia collision, Cenozoic climate, and geochemical weathering. GSA Bull. 130, 307–330. https://doi.org/10.1130/B31723.1.
Jellinek, A.M., Lenardic, A., Pierrehumbert, R.T., 2020. Ice, fire, or fizzle: the climate footprint of Earth's supercontinental cycles. Geochem. Geophys. Geosyst. 21, e2019GC008464. https://doi.org/10.1029/2019GC008464.
Jing, Z., Yu, W., Lewis, S., Thompson, L.G., Xu, J., Zhang, J., Xu, B., Wu, G., Ma, Y., Wang, Y., Guo, R., 2022. Inverse altitude effect disputes the theoretical foundation of stable isotope paleoaltimetry. Nat. Commun. 13, 4371. https://doi.org/10.1038/s41467-022-32172-9.
Kapp, P., DeCelles, P.G., 2019. Mesozoic–Cenozoic geological evolution of the Himalayan-Tibetan orogen and working tectonic hypotheses. Am. J. Sci. 319, 159–254. https://doi.org/10.2475/03.2019.01.
Khan, M.A., Spicer, R.A., Bera, S., Ghosh, R., Yang, J., Spicer, T.E.V., Guo, S., Su, T., Jacques, F., Grote, P.J., 2014. Miocene to Pleistocene floras and climate of the eastern Himalayan Siwaliks, and new palaeoelevation estimates for the Namling–Oiyug basin, Tibet. Glob. Planet. Change 113, 1–10. https://doi.org/10.1016/j.gloplacha.2013.12.003.
Li, J., Song, X., 2018. Tearing of Indian mantle lithosphere from high-resolution seismic images and its implications for lithosphere coupling in southern Tibet. Proc. Natl. Acad. Sci. 115, 8296–8300. https://doi.org/10.1073/pnas.1717258115.
Li, L., Garzione, C.N., 2017. Spatial distribution and controlling factors of stable isotopes in meteoric waters on the Tibetan Plateau: implications for paleoelevation reconstruction. Earth Planet. Sci. Lett. 460, 302–314. https://doi.org/10.1016/j.epsl.2016.11.046.
Li, S.-F., Valdes, P.J., Farnsworth, A., Davies-Barnard, T., Su, T., Lunt, D.J., Spicer, R.A., Liu, J., Deng, W.-Y.-D., Huang, J., Tang, H., Ridgwell, A., Chen, L.-L., Zhou, Z.-K., 2021. Orographic evolution of northern Tibet shaped vegetation and plant diversity in eastern Asia. Sci. Adv. 7, eabc7741. https://doi.org/10.1126/sciadv.abc7741.
Lippert, P.C., Zhao, X., Coe, R.S., Lo, C.-H., 2011. Palaeomagnetism and 40Ar/39Ar geochronology of upper Palaeogene volcanic rocks from central Tibet: implications for the central Asia inclination anomaly, the palaeolatitude of Tibet and post-50 Ma shortening within Asia. Geophys. J. Int. 184, 131–161. https://doi.org/10.1111/j.1365-246X.2010.04833.x.
Lunt, D.J., Farnsworth, A., Loptson, C., Foster, G.L., Markwick, P., O'Brien, C.L., Pancost, R.D., Robinson, S.A., Wrobel, N., 2016. Palaeogeographic controls on climate and proxy interpretation. Clim. Past 12, 1181–1198. https://doi.org/10.5194/cp-12-1181-2016.
Markwick, P.J., Valdes, P.J., 2004. Palaeo-digital elevation models for use as boundary conditions in coupled ocean–atmosphere GCM experiments: a Maastrichtian (late Cretaceous) example. Palaeogeogr. Palaeoclimatol. Palaeoecol. 213, 37–63. https://doi.org/10.1016/j.palaeo.2004.06.015.
Meyer, H.W., 2007. A review of paleotemperature–lapse rate methods for estimating paleoelevation from fossil floras. Rev. Mineral. Geochem. 66, 155–171. https://doi.org/10.2138/rmg.2007.66.6.
Molnar, P., 2005. Mio-Pliocene growth of the Tibetan Plateau and evolution of east Asian climate. Undefined.
Molnar, P., Boos, W.R., Battisti, D.S., 2010. Orographic controls on climate and paleoclimate of Asia: thermal and mechanical roles for the Tibetan Plateau. Annu. Rev. Earth Planet. Sci. 38, 77–102. https://doi.org/10.1146/annurev-earth-040809-152456.
Moore, M., Kuang, Z., Blossey, P.N., 2014. A moisture budget perspective of the amount effect. Geophys. Res. Lett. 41, 1329–1335. https://doi.org/10.1002/2013GL058302.
Poage, M.A., Chamberlain, C.P., 2001. Empirical relationships between elevation and the stable isotope composition of precipitation and surface waters: considerations for studies of paleoelevation change. Am. J. Sci. 301, 1–15. https://doi.org/10.2475/ajs.301.1.1.
Polissar, P.J., Freeman, K.H., Rowley, D.B., McInerney, F.A., Currie, B.S., 2009. Paleoaltimetry of the Tibetan Plateau from D/H ratios of lipid biomarkers. Earth Planet. Sci. Lett. 287, 64–76. https://doi.org/10.1016/j.epsl.2009.07.037.
Poulsen, C.J., Ehlers, T.A., Insel, N., 2010. Onset of convective rainfall during gradual late miocene rise of the central Andes. Science 328, 490–493. https://doi.org/10.1126/science.1185078.
Quade, J., Breecker, D.O., Daëron, M., Eiler, J., 2011. The paleoaltimetry of Tibet: an isotopic perspective. Am. J. Sci. 311, 77–115. https://doi.org/10.2475/02.2011.01.
Rowley, D.B., 2007. Stable isotope-based paleoaltimetry: theory and validation. Rev. Mineral. Geochem. 66, 23–52. https://doi.org/10.2138/rmg.2007.66.2.
Rowley, D.B., Currie, B.S., 2006. Palaeo-altimetry of the late Eocene to Miocene Lunpola basin, central Tibet. Nature 439, 677–681. https://doi.org/10.1038/nature04506.
Saupe, E.E., Farnsworth, A., Lunt, D.J., Sagoo, N., Pham, K.V., Field, D.J., 2019. Climatic shifts drove major contractions in avian latitudinal distributions throughout the Cenozoic. Proc. Natl. Acad. Sci. 116, 12895–12900. https://doi.org/10.1073/pnas.1903866116.
Shen, H., Poulsen, C.J., 2019. Precipitation δ^{18}O on the Himalaya–Tibet orogeny and its relationship to surface elevation. Clim. Past 15, 169–187. https://doi.org/10.5194/cp-15-169-2019.
Spicer, Robert A., Su, T., Valdes, P.J., Farnsworth, A., Wu, F.-X., Shi, G., Spicer, T.E.V., Zhou, Z., 2021a. The topographic evolution of the Tibetan region as revealed by palaeontology. Palaeobiodivers. Palaeoenviron. 101, 213–243. https://doi.org/10.1007/s12549-020-00452-1.
Spicer, Robert A., Su, T., Valdes, P.J., Farnsworth, A., Wu, F.-X., Shi, G., Spicer, T.E.V., Zhou, Z., 2021b. Why 'the uplift of the Tibetan Plateau' is a myth. Natl. Sci. Rev. 8, nwaa091. https://doi.org/10.1093/nsr/nwaa091.
Spicer, Robert A., Yang, J., Spicer, T.E.V., Farnsworth, A., 2021c. Woody dicot leaf traits as a palaeoclimate proxy: 100 years of development and application. Palaeogeogr. Palaeoclimatol. Palaeoecol. 562, 110138. https://doi.org/10.1016/j.palaeo.2020.110138.
Su, T., Farnsworth, A., Spicer, R.A., Huang, J., Wu, F.-X., Liu, J., Li, S.-F., Xing, Y.-W., Huang, Y.-J., Deng, W.-Y.-D., Tang, H., Xu, C.-L., Zhao, F., Srivastava, G., Valdes, P.J., Deng, T., Zhou, Z.-K., 2019. No high Tibetan Plateau until the Neogene. Sci. Adv. 5, eaav2189. https://doi.org/10.1126/sciadv.aav2189.
Su, T., Spicer, R.A., Wu, F.-X., Farnsworth, A., Huang, J., Rio, C.D., Deng, T., Ding, L., Deng, W.-Y.-D., Huang, Y.-J., Hughes, A., Jia, L.-B., Jin, J.-H., Li, S.-F., Liang, S.-Q., Liu, J., Liu, X.-Y., Sherlock, S., Spicer, T., Srivastava, G., Tang, H., Valdes, P., Wang, T.-X., Widdowson, M., Wu, M.-X., Xing, Y.-W., Xu, C.-L., Yang, J., Zhang, C., Zhang, S.-T., Zhang, X.-W., Zhao, F., Zhou, Z.-K., 2020. A middle Eocene lowland humid subtropical "Shangri-La" ecosystem in central Tibet. Proc. Natl. Acad. Sci. 117, 32989–32995. https://doi.org/10.1073/pnas.2012647117.
Tharammal, T., Bala, G., Noone, D., 2017. Impact of deep convection on the isotopic amount effect in tropical precipitation. J. Geophys. Res., Atmos. 122, 1505–1523. https://doi.org/10.1002/2016JD025555.
Tian, L., Yao, T., MacClune, K., White, J.W.C., Schilla, A., Vaughn, B., Vachon, R., Ichiyanagi, K., 2007. Stable isotopic variations in West China: a consideration of moisture sources. J. Geophys. Res., Atmos. 112. https://doi.org/10.1029/2006JD007718.
Tindall, J., Flecker, R., Valdes, P., Schmidt, D.N., Markwick, P., Harris, J., 2010. Modelling the oxygen isotope distribution of ancient seawater using a coupled ocean–atmosphere GCM: implications for reconstructing early Eocene climate. Earth Planet. Sci. Lett. 292, 265–273. https://doi.org/10.1016/j.epsl.2009.12.049.
Tindall, J.C., Valdes, P.J., Sime, L.C., 2009. Stable water isotopes in HadCM3: isotopic signature of El Niño–southern oscillation and the tropical amount effect. J. Geophys. Res., Atmos. 114. https://doi.org/10.1029/2008JD010825.
Utescher, T., Bruch, A.A., Erdei, B., François, L., Ivanov, D., Jacques, F.M.B., Kern, A.K., Liu, Y.-S.(C.), Mosbrugger, V., Spicer, R.A., 2014. The coexistence approach—theoretical background and practical considerations of using plant fossils for climate quantification. Palaeogeogr. Palaeoclimatol. Palaeoecol. 410, 58–73. https://doi.org/10.1016/j.palaeo.2014.05.031.
Valdes, P.J., Armstrong, E., Badger, M.P.S., Bradshaw, C.D., Bragg, F., Crucifix, M., Davies-Barnard, T., Day, J.J., Farnsworth, A., Gordon, C., Hopcroft, P.O., Kennedy, A.T., Lord, N.S., Lunt, D.J., Marzocchi, A., Parry, L.M., Pope, V., Roberts, W.H.G., Stone, E.J., Tourte, G.J.L., Williams, J.H.T., 2017. The BRIDGE HadCM3 family of climate models: HadCM3@Bristol v1.0. Geosci. Model Dev. 10, 3715–3743. https://doi.org/10.5194/gmd-10-3715-2017.
Valdes, P.J., Lin, D., Farnsworth, A., Spicer, R.A., Li, S.-H., Tao, S., 2019. Comment on "Revised paleoaltimetry data show low Tibetan Plateau elevation during the Eocene". Science 365, eaax8474. https://doi.org/10.1126/science.aax8474.
Valdes, P.J., Scotese, C.R., Lunt, D.J., 2021. Deep ocean temperatures through time. Clim. Past 17, 1483–1506. https://doi.org/10.5194/cp-17-1483-2021.
Walsh, K., 1994. On the influence of the Andes on the general circulation of the southern hemisphere. J. Climate 7, 1019–1025. https://doi.org/10.1175/1520-0442(1994)007<1019:OTIOTA>2.0.CO;2.
Wang, C., Dai, J., Zhao, X., Li, Y., Graham, S.A., He, D., Ran, B., Meng, J., 2014. Outward-growth of the Tibetan Plateau during the Cenozoic: a review. Tectonophysics 621, 1–43. https://doi.org/10.1016/j.tecto.2014.01.036.
Wang, C., Zhao, X., Liu, Z., Lippert, P.C., Graham, S.A., Coe, R.S., Yi, H., Zhu, L., Liu, S., Li, Y., 2008. Constraints on the early uplift history of the Tibetan Plateau. Proc. Natl. Acad. Sci. 105, 4987–4992. https://doi.org/10.1073/pnas.0703595105.
Xiong, Z., Ding, L., Spicer, R.A., Farnsworth, A., Wang, X., Valdes, P.J., Su, T., Zhang, Q., Zhang, L., Cai, F., Wang, H., Li, Z., Song, P., Guo, X., Yue, Y., 2020. The early Eocene rise of the Gonjo basin, SE Tibet: from low desert to high forest. Earth Planet. Sci. Lett. 543, 116312. https://doi.org/10.1016/j.epsl.2020.116312.
Xiong, Z., Liu, X., Ding, L., Farnsworth, A., Spicer, R.A., Xu, Q., Valdes, P., He, S., Zeng, D., Wang, C., Li, Z., Guo, X., Su, T., Zhao, C., Wang, H., Yue, Y., 2022. The rise and demise of the Paleogene central Tibetan valley. Sci. Adv. 8, eabj0944. https://doi.org/10.1126/sciadv.abj0944.
Yang, H., Shen, X., Yao, J., Wen, Q., 2020. Portraying the impact of the Tibetan Plateau on global climate. J. Climate 33, 3565–3583. https://doi.org/10.1175/JCLI-D-18-0734.1.
Yao, T., Masson-Delmotte, V., Gao, J., Yu, W., Yang, X., Risi, C., Sturm, C., Werner, M., Zhao, H., He, Y., Ren, W., Tian, L., Shi, C., Hou, S., 2013. A review of climatic controls on δ^{18}O in precipitation over the Tibetan Plateau: observations and simulations. Rev. Geophys. 51, 525–548. https://doi.org/10.1002/rog.20023.
Zhang, P., Najman, Y., Mei, L., Millar, I., Sobel, E.R., Carter, A., Barfod, D., Dhuime, B., Garzanti, E., Govin, G., Vezzoli, G., Hu, X., 2019. Palaeodrainage evolution of the large rivers of East Asia, and Himalayan-Tibet tectonics. Earth-Sci. Rev. 192, 601–630. https://doi.org/10.1016/j.earscirev.2019.02.003.